Progress in Oceanography 231 (2025) 103418

Contents lists available at ScienceDirect

Progress in Oceanography

journal homepage: www.elsevier.com/locate/pocean

Tidal energetics in the eddying South China Sea from a high-resolution numerical simulation

Yonghe Tian [a], Xiaolin Bai [a], Chuanyin Wang [b], Zhiyu Liu [a,*]

[a] State Key Laboratory of Marine Environmental Science, and Department of Physical Oceanography, College of Ocean and Earth Sciences, Xiamen University, Xiamen, China
[b] School of Atmospheric Sciences, Sun Yat-Sen University, Southern Marine Science and Engineering Guangdong Laboratory (Zhuhai), Zhuhai, China

ARTICLE INFO

Keywords:
Baroclinic tides
Energy budgets
Decay scale
Seasonal variability
South China Sea
MITgcm LLC4320

ABSTRACT

Understanding tidal energetics is crucial for comprehending complex oceanic processes in the South China Sea (SCS). Tidal energy budget in different parts of the world's oceans has been widely estimated, but the dissipation pathways of tidal energy in the eddying ocean remain elusive. Based on a well-validated high-resolution numerical simulation, this study provides an updated estimate of tidal energy budget in the SCS with the modulation of realistic background currents and stratification. It reveals that ~19.72% of barotropic tidal energy input in the Luzon Strait (LS) is converted to baroclinic tides, ~75.66% of which is transmitted out of the LS and the other ~24.34% is dissipated locally. Additionally, ~61.20% of barotropic tidal energy is transmitted into the SCS, and the other ~19.07% is dissipated locally. Analysis of barotropic tidal energy budget highlights significant work rate of K_1 tide-generating force in the SCS, whereas analysis of baroclinic tidal energy budget reveals the impacts of background fields on energy conversion from barotropic to baroclinic tides and energy dissipation of baroclinic tides. The seasonal variability of tidal dynamics and energetics further highlights the modulations by background fields. An exponential decay of baroclinic tidal energy flux with the distance from the generation site is revealed, and the decay scales for K_1 (northwestward and southwestward beam of M_2) baroclinic tide are estimated as 404 (195 and 127) km. A simple scaling of baroclinic tidal energy flux in the SCS, which may be used to characterize tidal mixing in large-scale ocean and climate models, is thus devised.

1. Introduction

Baroclinic tides (also known as internal tides), which are internal waves with tidal frequencies, are ubiquitous in the world's oceans. They are mainly generated by barotropic tidal currents interacting with rough bottom topographies, such as continental shelves, seamounts, ridges, and submarine canyons (Baines, 1982; Garrett and Kunze, 2007; Lamb, 1994; Wunsch, 1975). From the point view of energetics, barotropic tides fuel baroclinic tides, which in turn energize mixing processes to maintain the global ocean stratification and meridional overturning circulation (Egbert and Ray, 2000; Munk and Wunsch, 1998). Therefore, understanding the spatiotemporal variability of baroclinic tidal energy and its controlling factors is crucial for accurately modeling ocean dynamics (Alford, 2003; de Lavergne et al., 2019; Simmons et al., 2004).

Many factors such as underwater topography (Di Lorenzo et al., 2006), background currents and stratification (Kelly and Lermusiaux, 2016; Kerry et al., 2014a, 2014b; Müller, 2013; Xu et al., 2013), remotely generated waves (Kerry et al., 2013), double-ridge resonance (Buijsman et al., 2014), the Earth's rotation (Farmer et al., 2009), as well as other oceanic processes contribute to the complexity of tidal energetics. The Luzon Strait (LS), owing to steep submarine ridges and strong barotropic tidal currents, is particularly noteworthy as a hotspot for baroclinic tide generation and propagation into the South China Sea (Farmer et al., 2011; Niwa and Hibiya, 2004). The South China Sea (SCS) is unique for its mix of multiscale dynamical processes, including a sandwich-like circulation (Cai et al., 2020), energetic mesoscale eddies (Chen et al., 2011), and the Kuroshio intrusion (Nan et al., 2015; Zhang et al., 2017). These processes, especially the Kuroshio intrusion and its associated eddies, play a significant role in shaping the circulation and stratification around the LS, influencing the generation and propagation of baroclinic tides (Alford et al., 2015; Chang et al., 2019; Pickering et al., 2015). Therefore, the tidal energetics in the SCS, including the LS, deserve comprehensive attention.

Observations and numerical simulations have been used to quantify

* Corresponding author at: State Key Laboratory of Marine Environmental Science, Xiamen University, Xiamen, Fujian 361102, China.
E-mail address: zyliu@xmu.edu.cn (Z. Liu).

https://doi.org/10.1016/j.pocean.2025.103418
Received 17 August 2024; Received in revised form 10 November 2024; Accepted 5 January 2025
Available online 9 January 2025

tidal energetics in the SCS (Alford et al., 2011; Huang et al., 2018; Lien et al., 2014; Rainville et al., 2013). Obviously, it is impossible to map the basin-scale energetics in the SCS using sparse observations. Instead, satellite altimetry provides an efficient way to map the two-dimensional basin-scale distribution of low-mode (mostly mode-1) baroclinic tides (Ray and Zaron, 2011; Zhao, 2014; Zhao et al., 2016; Zhao and Qiu, 2023). However, only coherent baroclinic tides can be extracted from the altimeter data due to the long repeat cycle of the satellite, leading to an underestimate of the baroclinic tidal energy (Zaron and Egbert, 2014). Based on numerical simulations, previous studies have investigated tidal energetics in the SCS and shown widely varying results. Among them, some studies focused on the LS (Jan et al., 2008; Simmons et al., 2011), while some used horizontally homogeneous stratification without considering background currents (Kerry et al., 2013; Wang et al., 2016; Xu et al., 2016). Obviously, such idealized configurations cannot simulate realistic spatial–temporal variations of baroclinic tides modulated by multiscale dynamical processes, such as large-scale circulation, mesoscale eddies, fronts, and wave-wave interactions (Guo et al., 2023; Li et al., 2019; Wang et al., 2018; Wang et al., 2021). Although some recent studies have introduced realistic forcing into numerical simulations, the low resolution or climatological surface forcing makes it difficult to resolve the coupling of tidal dynamics with the complex dynamical environments in the SCS and the strong tidal energy dissipation in the LS (Buijsman et al., 2020; Song and Chen, 2020; Xu et al., 2021).

In this study, our objective is to investigate tidal energetics in the SCS using a high-resolution numerical simulation with realistic settings. We leverage the ECCO project's 1/48° LLC4320 simulation (Rocha et al., 2016), which incorporates astronomical tidal forcing and 6-hourly atmospheric forcing to capture both barotropic and baroclinic tidal activities embedded in the background of multiscale dynamical processes. By analyzing the results of the simulation, we seek to gain insights into the dissipation pathways of tidal energy in the SCS. The paper is structured as follows. In Section 2, we describe the LLC4320 simulation, and tidal energy equations used in our analysis. Section 3 presents the results of tidal energetics, and related energy budget, as well as their seasonal variability. Specifically, we devise a simple scaling for the baroclinic tidal energy flux in Section 3.5, which may be used to characterize tidal mixing in large-scale ocean and climate models. Subsequently, we discuss these results in comparison with previous idealized studies in Section 4. Finally, Section 5 summarizes our findings.

2. Model and Methods

2.1. The MITgcm LLC4320 simulation

The data used in this study are from the LLC4320 simulation output based on the Massachusetts Institute of Technology general circulation model (MITgcm; Marshall et al., 1997). This tide-resolving and submesoscale-permitting simulation is conducted using an Arakawa-C grid mesh with a horizontal grid spacing of 1/48° (approximately 2.3 km in the SCS). It comprises 90 vertical layers, with the layer thickness gradually increasing from 1 m near the surface to around 480 m near the bottom, reaching a maximum model depth of 7 km in the global ocean. The simulation is driven by astronomical tidal forcing in conjunction with 6-hourly atmospheric forcing. The astronomical tidal forcing encompasses the complete luni-solar tidal potential, while the atmospheric forcing is derived from the 0.14° (approximately 15 km) European Center for Medium Range Weather Forecasts (ECMWF) operational atmospheric reanalysis dataset. The simulation is marched forward in time every 25 s and outputs prognostic variables as instantaneous snapshots stored hourly for a duration of 14 months, spanning from September 2011 to November 2012. More details can be found from Arbic et al. (2018) and https://wwwcvs.mitgcm.org/viewvc/MITgcm/MITgcm_contrib/llc_hires/llc_4320/. Additionally, the LLC4320 simulation output analyzed in this study is openly available at https://data.nas.nasa.gov/ecco/data.php?dir=/eccodata/llc_4320.

The LLC4320 simulation is chosen for the present study because of four notable features that are lacking or less faithfully represented in previous studies. First, the high resolution of the LLC4320 simulation has not been reached by previous tidal studies in the SCS. Second, different from most studies in the SCS that prescribe barotropic tidal forcing at the open boundaries, the LLC4320 simulation considers the full luni-solar tidal potential as a body force in the momentum equations directly. This manner ensures the local generation of barotropic tides; more importantly, it straightforwardly allows the explicit calculation of the work rate done by the tide-generating force, which proved important for tidal energetics (Zu et al., 2008). Third, the output in the SCS, which is extracted from the global LLC4320 simulation, naturally considers the baroclinic tides propagating into or out of the SCS through the open boundaries. Recent studies emphasized that baroclinic tidal forcing imposed along the SCS open boundaries, although neglected in previous model-based studies, turns out to be non-negligible for the exploration of tidal energetics (Siyanbola et al., 2023; Siyanbola et al., 2024). Fourth, by employing 6-hourly atmospheric forcing, the LLC4320 simulation provides a more realistic representation of atmospheric conditions than utilizing climatological surface forcing. All the four features provide the potential to reproduce a more realistic oceanic environment with multiscale dynamical processes (from $O(10)$ km to basin scales) and their interactions. Lin et al. (2020) conducted a heavy validation of the LLC4320 simulation in the SCS and found that the large-scale circulation, mesoscale variability, submesoscale processes, barotropic tides, and internal gravity waves are quite faithfully simulated. Further quantitative evaluations of the LLC4320 simulation are described in the Discussion section. Therefore, the LLC4320 simulation is well-suited for investigating tidal energetics in the SCS. The specific study region spans from 105°E to 125°E and 5°N to 30°N. The bathymetry of the domain and several important topography features of the SCS are shown in Fig. 1. Typical months representing the summer (August) and winter (February) are analyzed to reveal seasonal variations. The baroclinic tidal energy is expected to be stronger in summer due to its strong stratification. Therefore, we mainly focus on the summer season when presenting the results of the tidal energetics and associated energy budgets in Section 3.1-3.5. But the seasonal variability of tidal energetics is also briefly examined by comparing the winter and summer scenarios in Section 3.6.

2.2. Tidal energy equations

Here we introduce the barotropic and baroclinic energy equations to diagnose tidal energetics (Gill, 1982; Niwa and Hibiya, 2004; Wang et al., 2016). Since the derivation of tidal energy equations is quite standard, only a brief introduction is presented here. First, we decompose the variables into a slowly varying background state and a perturbation component. The perturbation component captures the effects of both the barotropic and baroclinic tidal motions. For example, the horizontal velocity fields are divided as follows

$$u(z,t) = \overline{\mathbf{u}}(z,t) + \mathbf{u}'(z,t) = \overline{\mathbf{u}}(z,t) + \mathbf{u}'_{\mathrm{bt}}(t) + \mathbf{u}'_{\mathrm{bc}}(z,t), \tag{1}$$

$$\mathbf{u}'_{\mathrm{bt}}(t) = \frac{1}{H}\int_{-H}^{\eta} \mathbf{u}'(z,t)dz, \tag{2}$$

where $\mathbf{u} = (u, v)$ is the instantaneous horizontal velocity vector, $\overline{\mathbf{u}}$ represents the subtidal background velocity which is obtained by low-pass filtering $\mathbf{u}$ with a 3-day cutoff frequency, H is the mean water depth and η is the surface elevation at each grid. The instantaneous vertical velocity associated with barotropic tides can be expressed as

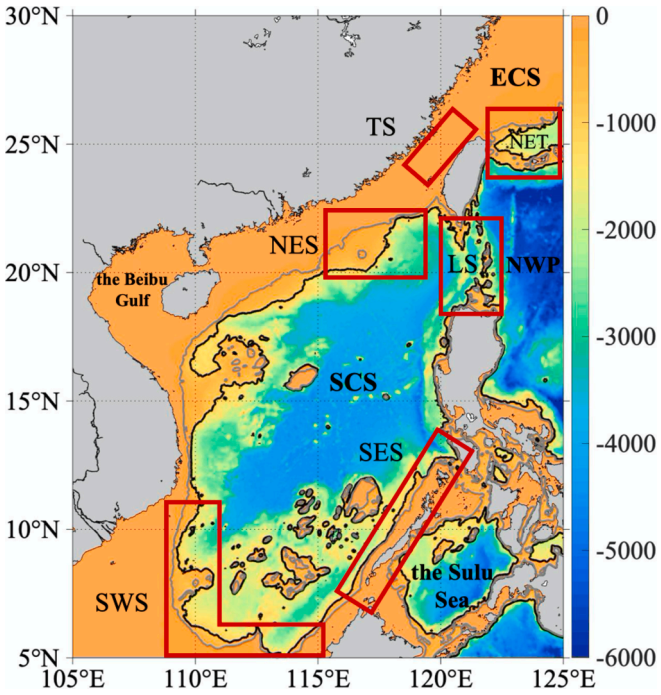

Fig. 1. Bathymetric map of the SCS employed in the LLC4320 simulation, where the colors indicate the water depth (Unit: m). The black and grey solid lines represent 1000-m and 200-m isobaths, respectively. Black bold texts represent the South China Sea (SCS), the northwest Pacific Ocean (NWP), the East China Sea (ECS) and the Sulu sea. And red boxes represent several important topography features, such as the Luzon Strait (LS), the Taiwan Strait (TS), northeastern shelf-slope area of Taiwan (NET), northeastern shelf-slope area of the SCS (NES), southwestern shelf-slope area of the SCS (SWS), southeastern shelf-slope area of the SCS (SES). (For interpretation of the references to color in this figure legend, the reader is referred to the web version of this article.)

$$\begin{cases} w'_{\mathrm{bt}}(\eta) = \dfrac{\partial \eta'_{\mathrm{bt}}}{\partial t} + \mathbf{u}'_{\mathrm{bt}} \cdot \nabla_h \left(\eta'_{\mathrm{bt}}\right), \\ w'_{\mathrm{bt}}(z) = w'_{\mathrm{bt}}(-H) - (z+H)\nabla_h \cdot \mathbf{u}'_{\mathrm{bt}}, \\ w'_{\mathrm{bt}}(-H) = \mathbf{u}'_{\mathrm{bt}} \cdot \nabla_h(-H). \end{cases} \tag{3}$$

A similar operation can be performed for the density fields, given by

$$\rho(z,t) = \overline{\rho}(z,t) + \rho'(z,t), \tag{4}$$

and the barotropic and baroclinic pressure fields can be expressed as

$$p'_{\mathrm{bt}}(t) = \frac{1}{H}\int_{-H}^{\eta} p'(z,t)dz = p'_{\mathrm{surface}}(t) + \frac{1}{H}\int_{-H}^{0}\int_{z}^{0} \rho'(\widetilde{z},t) g d\widetilde{z} dz, \tag{5}$$

$$p'_{\mathrm{bc}}(z,t) = p'(z,t) - p'_{\mathrm{bt}}(t) = \int_{z}^{\eta} \rho'(\widetilde{z},t) g d\widetilde{z} - \frac{1}{H}\int_{-H}^{0}\int_{z}^{0} \rho'(\widetilde{z},t) g d\widetilde{z} dz, \tag{6}$$

where

$$p'_{\mathrm{surface}}(t) = \rho_0 g \eta(t) - \frac{1}{T}\int_0^T \rho_0 g \eta(\widetilde{t}) d\widetilde{t}, \tag{7}$$

the constant reference density $\rho_0 = 1024 \mathrm{kg\,m^{-3}}$, and T is taken as 3 days here.

As such, the depth-integrated energetics equations for barotropic and baroclinic tides averaged over a tidal period are listed as follows respectively

$$\mathrm{DIS_{bt}} \approx W - Conv - \nabla_h \cdot \mathbf{F}_{\mathrm{bt}}, \tag{8}$$

$$\mathrm{DIS_{bc}} \approx Conv - \nabla_h \cdot \mathbf{F}_{\mathrm{bc}}. \tag{9}$$

where Conv is the energy conversion from the barotropic to baroclinic tides, $\mathbf{F}_{\mathrm{bt}}$ is the barotropic tidal energy flux, $\mathbf{F}_{\mathrm{bc}}$ is the baroclinic tidal flux, W is the work rate done by the tide-generating force, $\mathrm{DIS_{bt}}$ is the dissipation of barotropic tidal energy and $\mathrm{DIS_{bc}}$ is the dissipation of baroclinic tidal energy. All those terms can be calculated as

$$Conv = \int_{-H}^{\eta} \rho' g w'_{\mathrm{bt}} dz, \tag{10}$$

$$\mathbf{F}_{\mathrm{bt}} = \int_{-H}^{\eta} \mathbf{u}'_{\mathrm{bt}} p'_{\mathrm{bt}} dz, \tag{11}$$

$$\mathbf{F}_{\mathrm{bc}} = \int_{-H}^{\eta} \mathbf{u}'_{\mathrm{bc}} p'_{\mathrm{bc}} dz, \tag{12}$$

$$W = \rho g \mathbf{u}'_{\mathrm{bt}} H \cdot \nabla_h (\zeta_{SAL} + \zeta_E), \tag{13}$$

where ζ_{SAL} is the ocean self-attraction and loading and ζ_E is the combined tidal potential and Earth tide. Note that $\mathrm{DIS_{bt}}$ and $\mathrm{DIS_{bc}}$ are calculated as the residuals. Then, the local dissipation efficiency, q, defined as the ratio of the area-integrated dissipation of baroclinic tidal energy and area-integrated energy conversion from barotropic to baroclinic tides, can be calculated as

$$q = \frac{\int_s ds \langle \mathrm{DIS_{bc}} \rangle}{\int_s ds \langle \mathrm{Conv} \rangle}. \tag{14}$$

3. Results

3.1. Distributions of barotropic tidal energy

Barotropic tides are the energy sources of baroclinic tides, and thus knowledge of their energy distributions is essential for understanding the source regions and generation processes of baroclinic tides. Here, we present the distributions of monthly-averaged barotropic tidal energy fluxes for the four primary constituents (M_2, S_2, K_1, and O_1) in summer, calculated using Eq. (11).

It is clear from Fig. 2 that all the four primary tidal constituents propagate from the Northwest Pacific (NWP) towards the SCS. However, the diurnal and semidiurnal constituents exhibit distinct behaviors in both the SCS and the NWP. In the eastern LS, diurnal tides primarily propagate westward, entering the SCS through the LS. In contrast, semidiurnal constituents propagate northwestward, entering the SCS through both the LS and the Taiwan Strait (TS). Upon passing the straits, semidiurnal tidal energy fluxes diminish sharply, while diurnal energy fluxes penetrate throughout the basin, flowing out through the southern continental shelves, i.e., the Southwestern Shelf (SWS) and the Southeastern Shelf (SES). These distribution characteristics revealed from the LLC4320 simulation align with previous observations (Beardsley et al., 2004) and idealized numerical simulations (Wang et al., 2016; Xu et al., 2016; Zu et al., 2008).

The energy budgets of barotropic tides are shown in Fig. 3. When the dashed box encircling the LS in Fig. 3a is focused on, it is found that ~81.56% (~135.34 GW, black number in Fig. 3a) of all barotropic tidal energy input into the box enters through the eastern boundary from the NWP, and ~18.44% (~30.60 GW) enters through the northern boundary. In addition, ~55.90% (~92.76 GW) exits through the western boundary into the SCS and ~4.25% (7.05 GW) exits through the southern boundary. As a result, ~39.85% (~66.13 GW) remains in the LS, contributing to local dissipation and the generation of baroclinic tides. Though the barotropic tidal energy is mostly contributed by K_1 and M_2, the behavior of the K_1 and M_2 barotropic tides exhibits a significant difference in the LS. The divergence of the barotropic tidal energy fluxes for K_1 (~15 GW, blue number) is much smaller than that for M_2 (~25.12 GW, red number), whereas the work rate of K_1 tide-generating force (~0.99 GW) is slightly larger than that of M_2 (~0.27 GW). In addition, it is worth noting that the work rate of the K_1 tide-

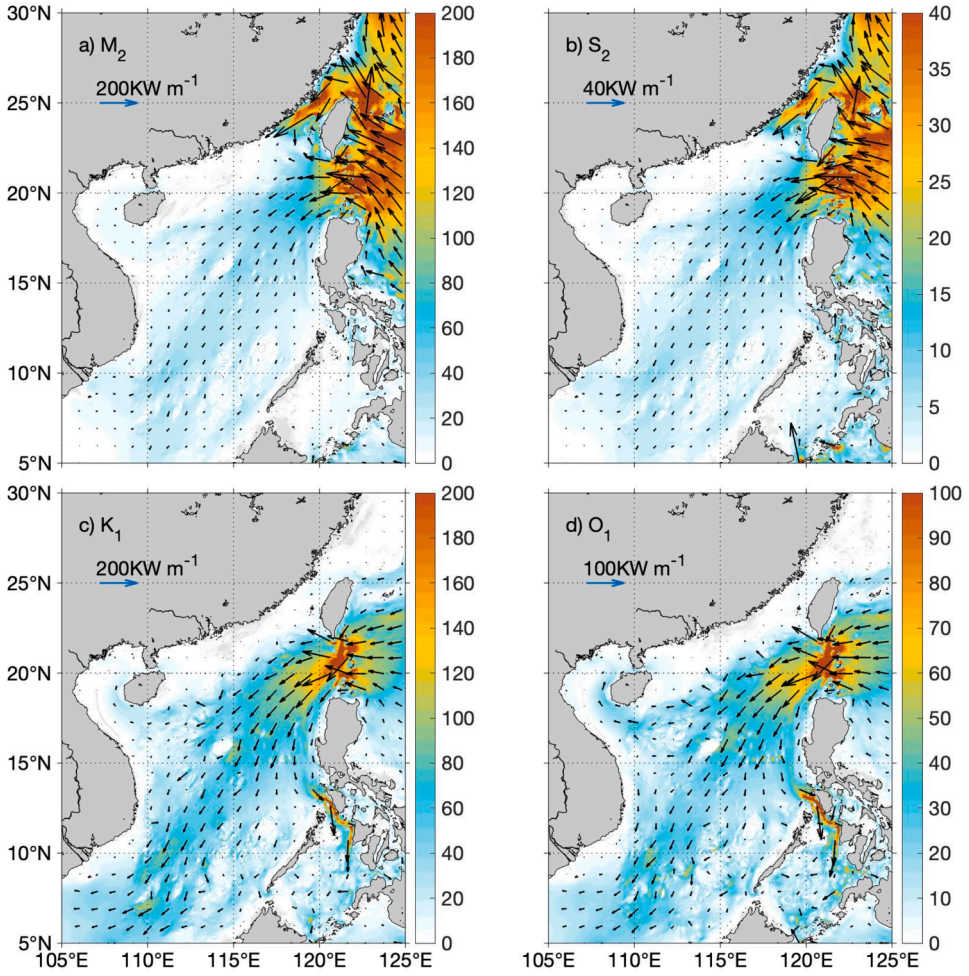

Fig. 2. The monthly-averaged barotropic tidal energy fluxes of the (a) M_2, (b) S_2, (c) K_1, and (d) O_1 constituents (Unit: KW m^{-1}) in summer. The colors represent the energy flux magnitudes, and the black arrows represent the energy flux vectors.

generating force in the LS is positive, whereas that for the M_2 in the LS is negative. These contrasting features indicate that K_1 (M_2) is energized (damped) by the tide-generating force. According to Eq. (13), the positive or negative of the work rate depends on the phase difference between barotropic velocity and tide-generating force, while the barotropic velocity contains not only the velocity of barotropic tides generated locally but also that of incident barotropic tides. Therefore, the positive work rate for K_1 does not mean that the K_1 barotropic tides are fully generated locally, and the negative work for M_2 seems to suggest that the M_2 barotropic tides are generated more remotely.

While in the SCS (Fig. 3b), ~99.63% (~103.67 GW) of all barotropic tidal energy input from the LS enters the SCS through the eastern boundary, ~42.78% (~44.51 GW) exits through the southwestern boundary, and ~16.72% (~17.40 GW) exits through the southeastern boundary, with ~40.51% (~42.15 GW) remaining in the SCS. Similar to the LS, the work rate of tide-generating force for K_1 in the SCS is positive, whereas that for M_2 is negative. In addition, the magnitude of the K_1 work rate (~1.45 GW) is much larger than that of the M_2 work rate (~0.06 GW), indicating that the work rate of the tide-generating force plays a more significant role for K_1 than M_2 in the SCS.

For K_1 in the SCS (Fig. 3b), the work rate constitutes approximately 20% of the divergence of the energy flux, and is much larger than the conversion from the barotropic to the baroclinic tides. These results highlight the substantial contribution of the work rate of the tide-generating force for K_1 to the tidal energy budget in the SCS. Note that the explicit inclusion of full luni-solar tidal potential in the governing equations of the LLC4320 simulation has allowed the calculation of the work rate done by the tide-generating force. Such calculation was not possible in most regional numerical simulations which only applied barotropic tidal forcing at the open boundaries (e.g., Wang et al., 2016; Xu et al., 2016; Wang et al., 2018). The significant contribution of the work rate of the tide-generating force to the tidal energy budget in the SCS was also revealed from previous barotropic tidal simulations (Zu et al., 2008). The necessity of explicitly incorporating full luni-solar tidal potential into the governing equations of tidal models is thus highlighted.

3.2. Characteristics of baroclinic tides

To explore the distribution of the baroclinic tides in a realistic ocean environment, we analyze the spatial distributions of near-surface pressure perturbations (Fig. 4). The presence of multi-wave interference patterns indicates the existence of multiple generation sources due to the complex topography of the SCS, with the LS identified as the main source. In Fig. 4a, instantaneous near-surface pressure perturbations around the LS exceed 1000 Pa, corresponding to a sea surface deflection of more than 150 mm. However, this perturbation rapidly decreases upon reaching the 200-m isobath. These characteristics are consistent with the patterns revealed by idealized simulations (Wang et al., 2016).

The M_2 beams (Fig. 4b) bifurcate into northwestward and southwestward directions. The stronger northwestward beam propagates towards the northern continental shelf, and the weaker southwestward beam propagates in a straight line without being significantly affected by the complex topography, which remains subcritical for the M_2 tide. In

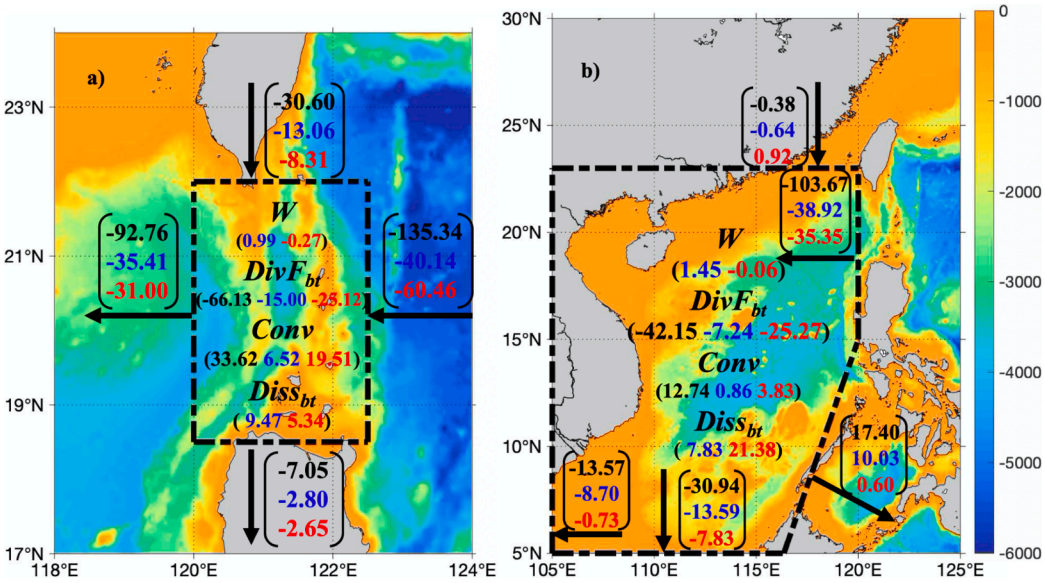

Fig. 3. Energy budgets of the barotropic tides in (a) the LS and (b) the SCS in summer, including the work rate done by the tidal generating force integrated in the regions within the dashed box (W, Unit: GW), the integrated divergence of the barotropic energy flux ($DivF_{bt}$, Unit: GW), the integrated energy conversion from the barotropic to baroclinic tides (Conv, Unit: GW), the integrated dissipation rate of barotropic tides ($Diss_{bt}$, Unit: GW), the energy flux integrated along the boundaries of dashed box (Unit: GW). The numbers are integrated results and the black dashed boxes represent the integrated areas. The black, blue, and red numbers represent all barotropic tides, K_1 tide and M_2 tide, respectively. The color shows the bathymetry. (For interpretation of the references to color in this figure legend, the reader is referred to the web version of this article.)

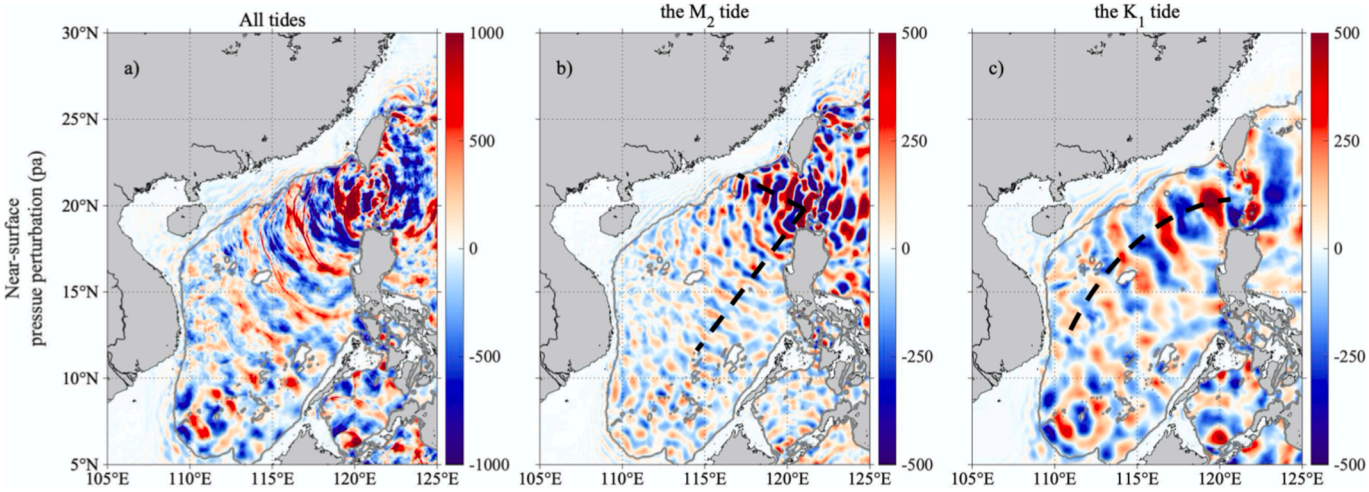

Fig. 4. The instantaneous near-surface pressure perturbation of (a) all baroclinic tides, (b) M_2 tide, (c) K_1 tide during the spring tide in summer. The black dashed lines denote the central paths of the M_2 and K_1 baroclinic tidal beams and the grey solid lines represent 200-m isobaths.

contrast, there is only one single beam for K_1 (Fig. 4c), which propagates westward from the LS, subsequently bends southwestward across the deep central basin and interferes with baroclinic tides generated from the SWS.

The amplitude of both the M_2 and K_1 tides decreases as they propagate away from the LS, with distinct crests disappearing around 15°N. For the M_2 tide, the amplitude decreases more rapidly during southwestward propagation than the northwestward propagation. For example, the near-surface pressure perturbation of the M_2 tide near the LS reaches ~956 Pa, decreasing rapidly along their southwestward propagation path to ~338 Pa at approximately 117.9°E, 16.3°N. However, due to the nonlinear steepening during shoaling, the near-surface pressure perturbation increases slightly along the same distance of southwestward propagation, remaining at ~635 Pa. Additionally, the wavelength near the LS is ~348 km for the K_1 tide and ~174 km for the M_2 tide. While the wavelength of K_1 decreases along the beam path, the wavelength of M_2 remains largely unchanged. This feature is caused by the Earth's rotation; that is, the phase speed is dependent on both the tidal frequency and the inertial frequency (Zhao, 2014). The inertial frequencies in the SCS are quite close to the tidal frequency of K_1 compared to M_2, indicating that the phase speed and the wavelength of K_1 are more susceptible to the latitudes in the SCS. Therefore, one can see the curved path of the K_1 beam in Fig. 4c (Zhao, 2014).

3.3. Distributions of baroclinic tidal energy

To gain a comprehensive insight into the baroclinic tides, we show the spatial distributions of the monthly-averaged tidal energetics (e.g., energy conversion, energy flux and dissipation) of the baroclinic tides (e.g., all baroclinic tides, K_1 tide, M_2 tide, and the residual constituent) in

summer (Fig. 5). Specifically, the residual constituent removes the diurnal (0.90–1.15 cpd) and semidiurnal (1.70–2.20 cpd) constituents from the whole baroclinic tidal fields.

It is evident from Fig. 5a-5d that the energy conversion from the barotropic to baroclinic tides can be either positive or negative; a positive conversion indicates that the baroclinic tides gain energy from the barotropic tides, whereas a negative conversion signifies energy loss from the baroclinic tides to the barotropic tides, attributed to phase differences between the barotropic vertical velocity and the baroclinic density perturbation (Eq. (10)). These phase differences, mainly caused by incident baroclinic tides, imply multiple generation sources of baroclinic tides. The LS is the main source of baroclinic tides, but also with local energy conversion from the baroclinic to barotropic tides. Apart from the LS, a small portion of the diurnal baroclinic tides are generated along the Zhongsha archipelago, the SWS, and the SES, consistent with the southwestward long-distance propagation of diurnal barotropic tides. In contrast, significant semidiurnal baroclinic tides are generated along complex topography, including the Ryukyu trench northeast of Taiwan and the shelf-slope southwest of Taiwan, associated with strong propagation beams of semidiurnal barotropic tides. However, the conversion is notably small on most continental shelves for both tidal constituents, especially in regions onshore the 200-m isobath. The northeastern shelf is a strong source region for the residual constituent of baroclinic tides, which may be due to the nonlinear interactions between the diurnal and semidiurnal baroclinic tides originating from the LS during their northwestward propagation, or interactions with the topography.

Baroclinic energy flux provides essential information on tidal propagation variability (Ansong et al., 2017; Wang et al., 2021; Xu et al., 2021), hence quantification of the energy flux in a realistic ocean environment is crucial. The energy fluxes of all baroclinic tides exhibit relatively regular tidal beam from the LS, and could exceed 60 KW m^{-1} near the source region. Consistent with the near-surface pressure perturbation described in the last section, the energy fluxes of the semidiurnal and diurnal baroclinic tides exhibit remarkably different propagation patterns (Fig. 5e-5h). The M_2 tide displays more branches than the K_1 tide; although the energy fluxes of K_1 are weaker than that of M_2 in the LS, the energy fluxes of the M_2 tide decay rapidly away from the LS, while the K_1 tide can travel over long distances.

As shown in Fig. 5i-5l, the energy dissipation of baroclinic tides generally mirrors the pattern of the energy conversion from the barotropic to baroclinic tides across most regions. This suggests that strong conversion is consistently accompanied by significant energy dissipation. However, some exceptions are notable, such as the dissipation of the M_2 tide on the northeastern shelf and the dissipation of the residual constituent of baroclinic tides in the LS. The energy conversion from the barotropic to baroclinic tides of the M_2 baroclinic tide is small on the northeastern shelf, while its energy dissipation is huge there. This

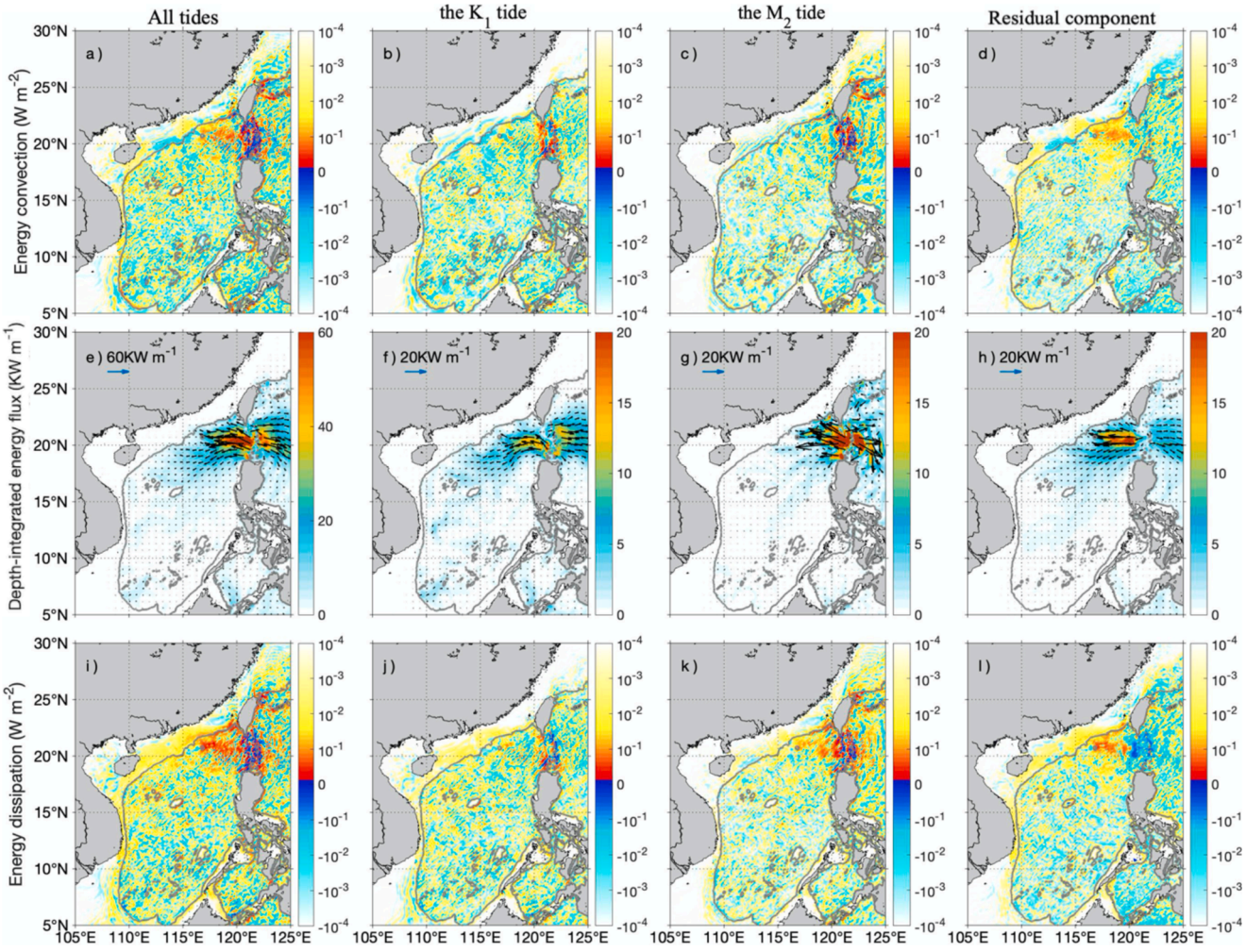

Fig. 5. The monthly-averaged baroclinic tidal energy in summer. (a)-(d) the conversion from barotropic to baroclinic tides, (e)-(h) the baroclinic energy flux, (i)-(l) the energy dissipation. The four columns present all baroclinic tides, K_1 tide, M_2 tide, and the residual constituent, respectively. In particular, the residual constituent removes the diurnal (0.90–1.15 cpd) and semidiurnal (1.70–2.20 cpd) constituents from the whole baroclinic tidal fields. The grey solid lines represent 200-m isobaths.

phenomenon indicates that the M_2 baroclinic tide, which is generated on the eastern ridge of the LS, propagates westward and dissipates primarily from the western ridge to the northeastern shelf-slope. In addition, the energy conversion from the barotropic to baroclinic tides for the residual constituent of baroclinic tides is small in the LS, while there is a significant negative energy dissipation, which is probably due to the energy transfer through nonlinear interactions. In the LS, the energy dissipation of the M_2 baroclinic tide is notably larger than that of the K_1 baroclinic tide; this is attributable to the specific wavelength of the M_2 baroclinic tide, which facilitates resonance between the two ridges (Alford et al., 2011). Moreover, combined with the energy fluxes (Fig. 5j and 5k), the energy dissipation (Fig. 5f and 5g) also shows that the K_1 tide can propagate thousands of kilometers into the deep basin, while the energy level of the M_2 tide diminishes sharply before reaching the Dongsha Plateau. In contrast to the distribution of the energy conversion, stronger dissipation occurs along the shallow shelves than in the deep basin, except for areas with rough topography.

3.4. Region-integrated energy budgets of baroclinic tides

We now investigate the region-integrated energy budgets of baroclinic tides within the LS and the SCS. A visual representation is shown in Fig. 6, and a concise overview summarizing the barotropic and baroclinic tidal energy budgets is given in Fig. 7.

In the LS (Fig. 6a), the energy fluxes through the northern and southern boundaries are one order smaller than those through the western and eastern boundaries, which could be negligible. ~33.62 GW (black number) is converted from barotropic tides to baroclinic tides, ~40.04% (~13.53 GW) of which exits through the western boundary into the SCS, and ~31.23 % (~10.50 GW) enters the NWP through the eastern boundary, with ~24.34% (~8.18 GW) dissipated locally. Although the energy conversion from the barotropic to baroclinic tides for M_2 (~19.51 GW, red number) is much larger than that for K_1 (~6.52 GW, blue number), the divergence of the energy fluxes for M_2 (~7.29 GW) is close to that for K_1 (~5.95 GW), indicating that a greater proportion of the baroclinic tidal energy generated in the LS is dissipated locally for M_2 (~62.12%, ~12.12 GW) than K_1 (~8.74%, ~0.57 GW).

In the SCS (Fig. 6b), the tidal energy fluxes through the SWS, SES, and TS are generally negligible compared to those from the LS. The divergences of the energy fluxes for all baroclinic tides (~13.01 GW, black number in Fig. 6b) and M_2 (~3.74 GW, red number) are comparable to their energy conversion from the barotropic to baroclinic tides (~12.74 GW, ~3.83 GW), respectively. Notably, the divergence of the energy fluxes for K_1 (~2.33 GW, blue number) is much larger than its energy conversion from the barotropic to baroclinic tides (~0.86 GW), indicating the significance of energy input from the LS on the baroclinic tidal energy budget in the SCS.

The concise overview summary of the barotropic and baroclinic tidal energy budgets is shown in Fig. 7. Taking the barotropic tidal energy transported into the LS from the NWP as 100%, ~61.20% is subsequently transported into the deep basin of the SCS. And ~19.72% barotropic tidal energy is converted to the baroclinic tides, and the other ~19.07% is dissipated locally within the LS. For the barotropic tidal energy input into the SCS (~61.20%), ~36.32% traverses the deep basin and flows out through the SWS and the SES, while only ~7.47% is converted to the baroclinic tides in the SCS and the other ~17.25% dissipated locally.

The behavior of the K_1 and M_2 barotropic tides exhibits a significant difference. Within the LS, ~41.75% is transported into the area from the NWP for M_2. In particular, ~14.58% remains in the LS, while the other ~27.01% is transmitted to the SCS. While, for K_1 more proportion of energy (~22.87%) is transmitted to the SCS, with only ~9.38% retained in the LS. This contrast may be attributed to the specific wavelength of the M_2 barotropic tide, which results in enhanced tidal dissipation and conversion when interacting with the topography, as suggested by Zu et al. (2008). Similarly, ~27.01% barotropic energy is transported into the SCS from the LS for M_2, and more of this energy remains in the SCS, which is either dissipated (~12.54%) or converted into baroclinic tides (~2.25%). In contrast, for the barotropic energy input from the LS (~22.87%) for K_1, more of this energy (~18.96%) is transmitted out of the SCS through the SWS and SES. Additionally, a higher proportion of the barotropic energy loss in the LS (~11.45%) is converted to baroclinic tides for M_2, whereas more of that (~5.56%) is dissipated locally for the K_1 tide.

For the baroclinic tides, more baroclinic energy generated in the LS is transmitted to the SCS (~8.47%), while other ~6.46% is transmitted

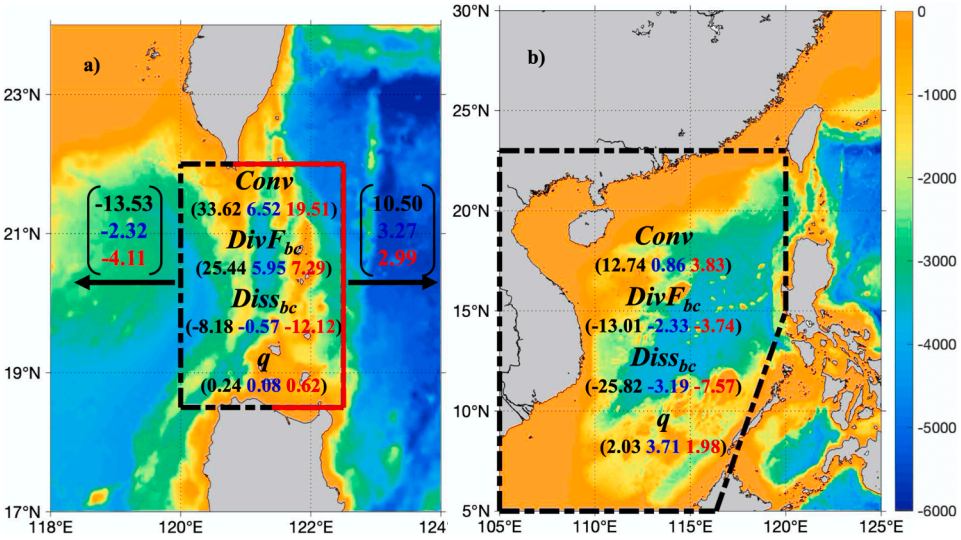

Fig. 6. Energy budgets of the baroclinic tides in (a) the LS and (b) the SCS in summer, including the energy conversion from the barotropic to baroclinic tides integrated in the regions within the dashed box (Conv, Unit: GW), the integrated divergence of the baroclinic energy flux ($DivF_{bc}$, Unit: GW), the integrated energy dissipation of baroclinic tides ($Diss_{bc}$, Unit: GW), the energy flux integrated along the boundaries of dashed box (Unit: GW), the local dissipation efficiency (q). The numbers are integrated results and the black dashed boxes represent the integrated areas. The black, blue and red numbers represent the baroclinic tides, the K_1 tide and the M_2 tide, respectively. The baroclinic energy fluxes across the north and south boundaries are one order of magnitude smaller than those through the western and eastern boundaries in the LS, which are not shown here (Song and Chen, 2020; Xu et al. 2021). (For interpretation of the references to color in this figure legend, the reader is referred to the web version of this article.)

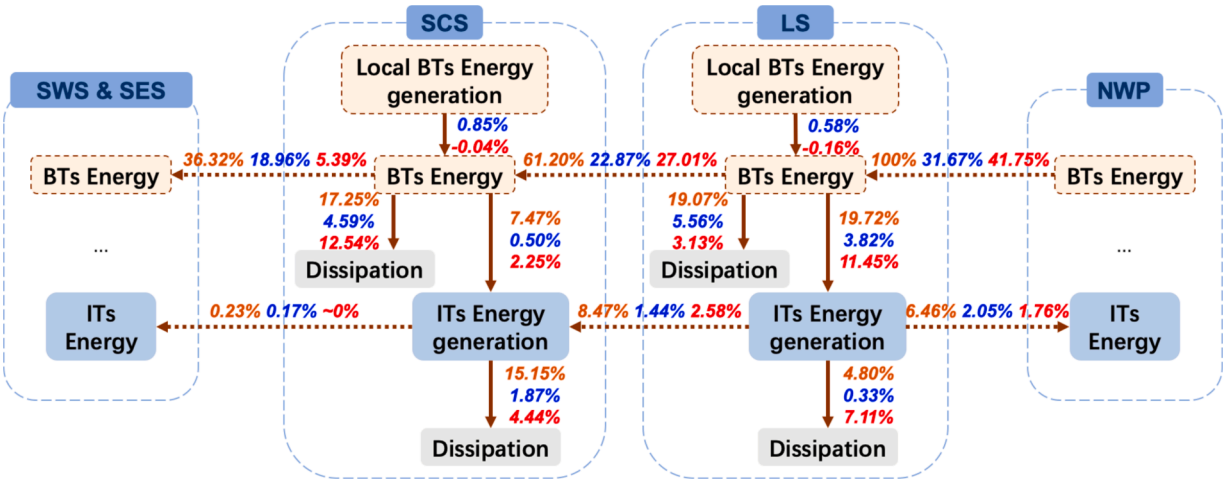

Fig. 7. An overview of the tidal energy budget within the LS and the SCS, assuming the barotropic energy transported into the LS from the NWP is 100%, the integration boundaries of which are shown in Fig. 6a with red solid lines. The "BTs" stands for the barotropic tides and the "ITs" stands for the internal (baroclinic) tides. The tawny, blue and red numbers represent the percentage of energy for all tides, the K_1 tide and the M_2 tide, respectively. The dashed lines indicate the energy transport, such as the barotropic or baroclinic energy flux between different regions. And the solid lines represent the energy transfer, such as the work rate done by the tidal generating force, the energy conversion from the barotropic to baroclinic tides, or the dissipation rate. (For interpretation of the references to color in this figure legend, the reader is referred to the web version of this article.)

back to the NWP, with the remaining ~4.80% dissipated locally. In the SCS, nearly all of the baroclinic tidal energy, including both the locally generated (~7.47%) and that transmitted from the LS (~8.47%), is dissipated locally (~15.15%), with only a small fraction (~0.23%) transmitted out from the southern shelf.

The behavior of the K_1 and M_2 baroclinic tides is also markedly different. The majority of the M_2 baroclinic energy generated in the LS is dissipated locally (~7.11%), with the remaining ~2.58% transmitted into the SCS and ~1.76% back to the NWP. In contrast, for the K_1 baroclinic tide, the majority of the converted baroclinic energy is transmitted to the SCS (~1.44%) and back to the NWP (~2.05%), with only a small fraction (~0.33%) dissipated in the LS. While in the SCS, together with the locally generated (~2.25%, ~0.50%) and that transmitted from the LS (~2.58%, ~1.44%), nearly all baroclinic tidal energy (~4.44%, ~1.87%) is dissipated locally, with only a negligible fraction (~0%, ~0.17%) transmitted out from the southern shelf for M_2 and K_1, respectively.

3.5. The decay scale of the baroclinic tidal energy flux

As mentioned in Section 3.2, there exist dominant beams, also visually displayed in Fig. 8a and 9a, for the propagation of baroclinic tides generated in the LS. Along the beam of K_1 (Fig. 8b), the baroclinic tide primarily propagates southwestward away from the LS. The magnitude of energy flux (the energy fluxes are projected onto the beam and integrated over the cross section) first experiences a successive decrease. Then it slightly increases when the K_1 baroclinic tide reaches approximately 300 km from the source region. This behavior may result from the tide's perpendicular propagation directions to the isobath around the Dongsha Islands. Subsequently, the energy flux decreases till around 600 km and 900 km of propagation, where the K_1 baroclinic tide interacts with the steep topography of the Zhongsha Islands and the continental shelf, resulting in two slight increases in energy flux. This result aligns with the high energy conversion from the barotropic to baroclinic tides as presented above. The negative value between 1200

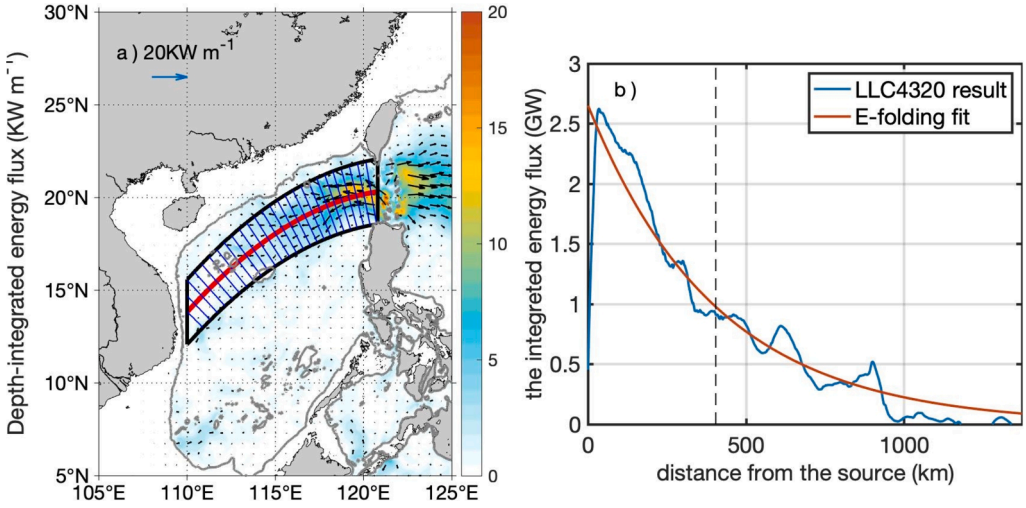

Fig. 8. The decay scale of the K_1 baroclinic tidal energy flux. (a) Energy flux of the K_1 baroclinic tide. The red solid-line represents the propagating beam, the black solid-lines represent the area used to calculate the decay scale, and the blue solid-lines represent the cross sections for integrating. (b) The section integrated baroclinic energy flux along-propagation distance from the source region. The black dashed-line represents the decay scale of the K_1 baroclinic tidal energy flux. (For interpretation of the references to color in this figure legend, the reader is referred to the web version of this article.)

km and 1300 km may result from reflections following interactions with topography in the continental shelf location. Although the baroclinic tidal energy flux varies in a complicated way along the beam, it in general decays exponentially with the along-propagation distance from the source region. Thus, the variability of the energy flux for the K_1 baroclinic tide can be described by a monotonically decaying function, which motivates an exponential fitting as follows

$$F_{K_1} = F_{0K_1} e^{-x/L_{K_1}}. \tag{15}$$

Here, x is the along-propagation path distance from the source region in the unit of km, $F_{0K_1} = 2.65$ GW is for the amplitude of energy flux, and $L_{K_1} = 404$ km represents the decay scale of the K_1 baroclinic tide.

The M_2 baroclinic tide bifurcates into northwestward and southwestward directions, thus we conduct integration along the two beams separately (Fig. 9). Compared to the K_1 baroclinic tide, the integrated energy flux of the M_2 baroclinic tide is substantially higher at the source regions but decreases rapidly upon exiting the LS. For the stronger northwestward beam (Fig. 9a-b), the integrated energy flux reaches two peak values at locations near the source. The first peak is due to the strong M_2 baroclinic tide generated by the East Ridge (~10 km from the source) in the LS, and the second peak is a result of the slightly weaker M_2 baroclinic tidal energy generated by the West Ridge (~55 km from the source). As the M_2 baroclinic tide exits the LS, its integrated energy flux decreases rapidly. Subsequently, a significant increase exists around 130 km of propagation due to the topographic shoaling of the northeastern continental shelf. In addition, one can see that another distinct increase occurs around 330 km from the source where the M_2 baroclinic tide interacts with the steeply sloping terrain of the Dongsha Islands. Similar to K_1, the variability of the energy flux for the stronger northwestward beam of the M_2 baroclinic tide can also be described by an exponential fitting (Fig. 9b), that is

$$F_{M_2\_nw} = F_{0M_{2\_nw}} e^{-x/L_{M_{2\_nw}}}. \tag{16}$$

Here, $F_{0M_{2\_nw}} = 5.8$ GW represents the amplitude of energy flux of the northwestward beam of the M_2 baroclinic tide. The decay scale $L_{M_{2\_nw}} =$ 195 km, which is about half of that for K_1.

For the weaker southwestward beam of M_2 (Fig. 9c-d), the integrated energy flux decays more rapidly than the northwestward beam. In particular, as soon as it transmits out from the LS (~240 km from the source), the integrated energy flux drops almost to zero. However, there is a slight increase when passing south of the eastern ridge (~127 km from the source), where the M_2 baroclinic tide is also generated. Similarly, an exponential fitting of the energy flux for the weaker southwestward beam gives

$$F_{M_2\_sw} = F_{0M_{2\_sw}} e^{-x/L_{M_{2\_sw}}}, \tag{17}$$

where $F_{0M_{2\_sw}} = 6.28$ GW and $L_{M_{2\_sw}} = 127$ km. The decay scale of the southward beam of the M_2 baroclinic tide is about 65% of that of the northwestward beam.

3.6. Seasonal variability of tidal energetics

The analyses of tidal energetics presented above are focused on the

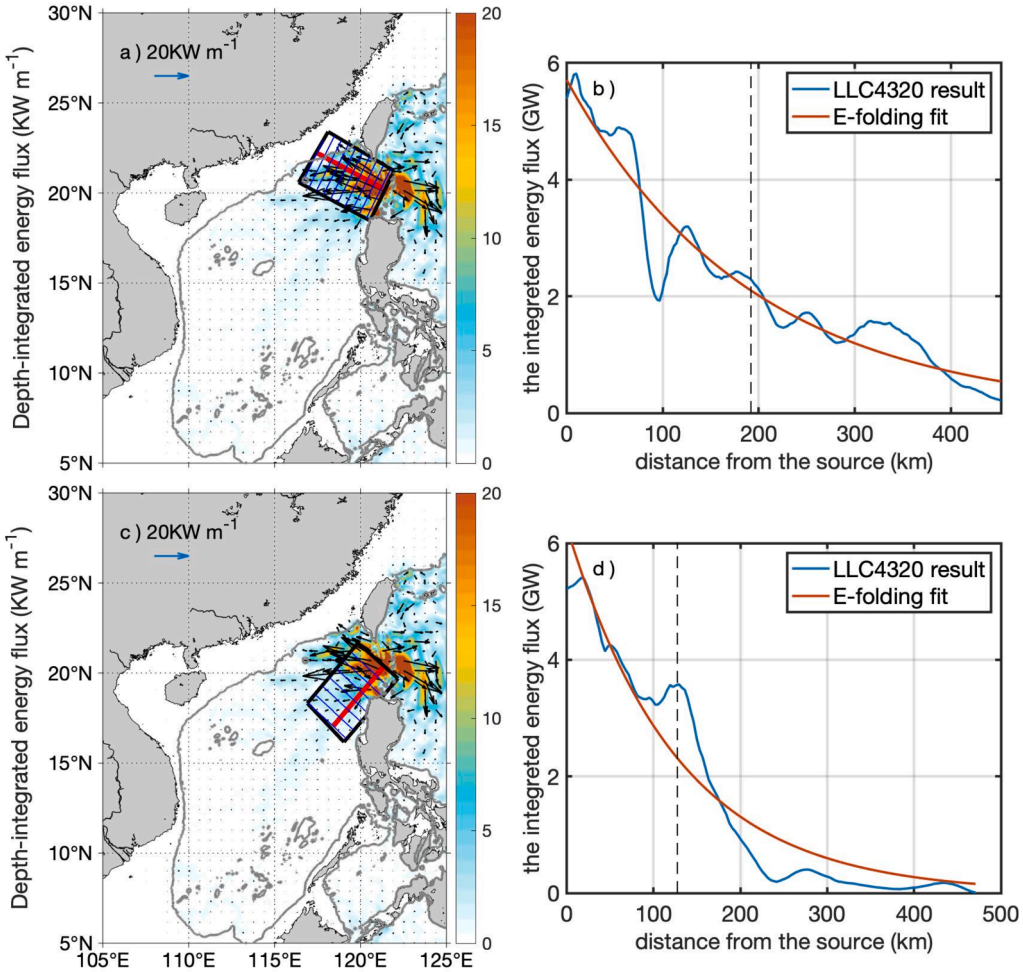

Fig. 9. Same as Fig. 8, but for the M_2 baroclinic tide. (a) and (b) calculate the area covering the northwestward propagating beam. (c) and (d) calculate the area covering the southwestward propagating beam.

summer, i.e., the monthly average in August. In the SCS, the background currents and stratification are seasonally modulated by the monsoon, as well as the Kuroshio intrusion and its associated eddies, which are expected to further induce seasonal variations of both the characteristics and energetics of baroclinic tides. Therefore, the baroclinic tidal amplitudes, as well as each term in the baroclinic energy equation, are checked to investigate whether there is indeed a significant difference between summer and winter.

Distinct patterns in the circulation during the summer (August) and winter (February) are shown in Fig. 10a-b, illustrating a leaping path and stronger stratification within the upper 200-m thermocline in summer, and a looping path with weaker stratification in winter. To delve into the tidal characteristics, we analyze model output at a location (20.25°N, 121.3°E) where baroclinic tides are strongly generated. In Fig. 10e-f, the amplitude of baroclinic tides remains similar during the neap tide for the two seasons, measuring 56.9 m in summer and 51.9 m

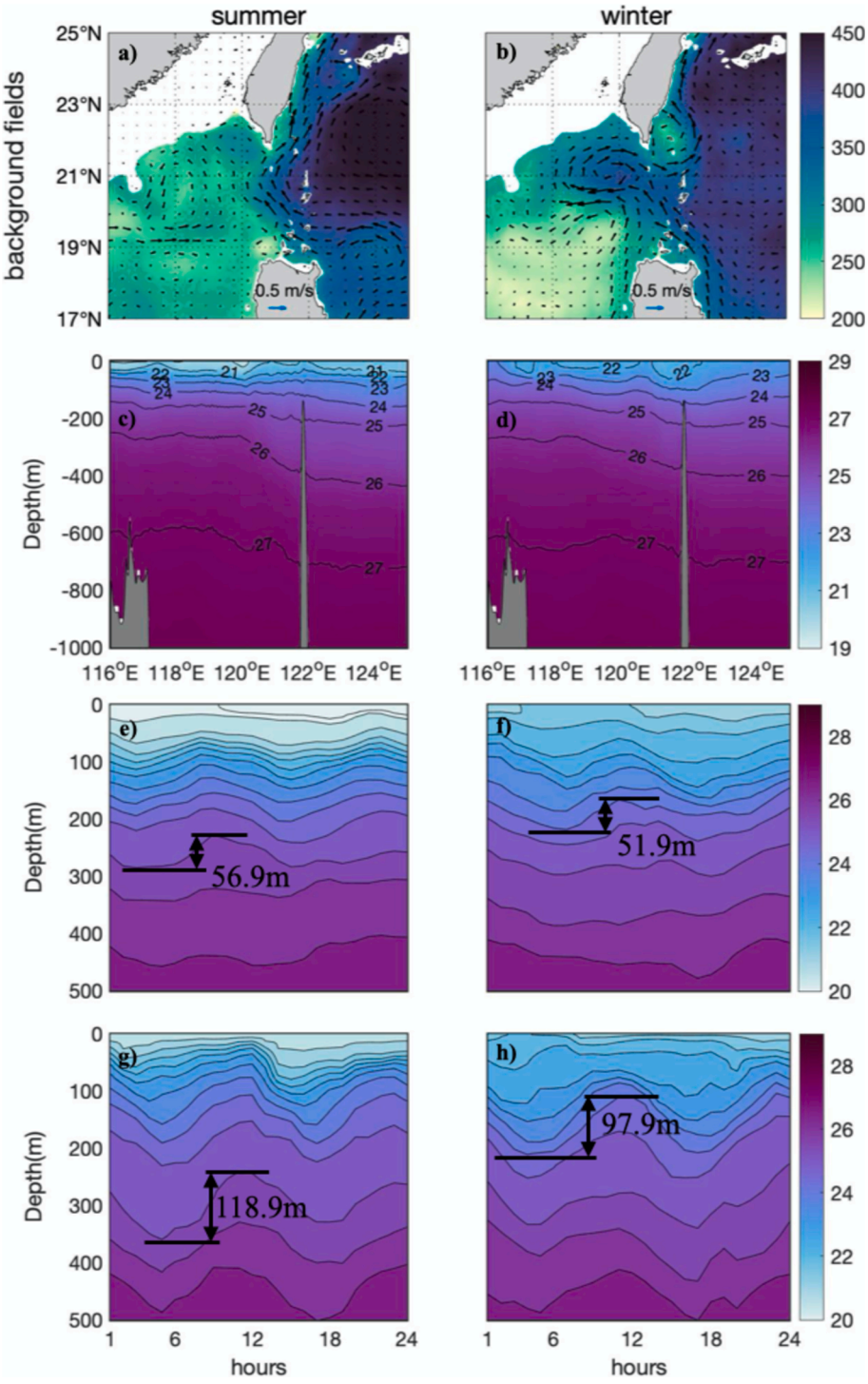

Fig. 10. (a)-(b) The background fields during one tidal period of two seasons. The color contours represent the depth of the 1026 kg m^{-3} isopycnal (Unit: m). The black arrows represent the depth-averaged background currents in the upper 500 m (Unit: m s^{-1}). (c)-(d) The potential density (minus 10^3 kg m^{-3}) in the upper 1000-m layer along 20.25°N (Unit: kg m^{-3}). (e)-(f) The time-series of potential density (minus 10^3 kg m^{-3}) in the upper 500-m layer at 121.3°E, 20.25°N during the neap tide period (Unit: kg m^{-3}). The numbers represent the largest isopycnal displacements. (g)-(h) Same as (e)-(f) but during the spring tide period.

in winter. However, they exhibit a substantial difference of approximately 20 m during the spring tide, as depicted in Fig. 10g-h. Isopycnals in summer appear more clustered in the upper 200-m layer, with an amplitude of 118.9 m. We further calculate the meridional integrated energy conversion from the barotropic to baroclinic tides for the two seasons, with the integrated area spanning from 17°N to 25°N. As shown in Fig. 11, the spatial distribution of the energy conversion from the barotropic to baroclinic tides remains similar, with high values concentrated around the two ridges in the LS, indicating hotspots of the generation of baroclinic tides. One can see that there are no distinct differences of the tidal energy conversion between the two seasons along the 20.25°N, with similar baroclinic tidal energy despite changes in background currents and stratification. The minor energy discrepancy alongside the considerable displacement difference in the two seasons further suggests the importance of considering background currents and stratification in baroclinic tidal dynamics and energetics, as noted by Zhao and Qiu (2023).

Besides, the energy fluxes of baroclinic tides also exhibit a huge difference between the summer and winter. As shown in Fig. 12, not only the magnitude of energy fluxes but also the propagation path shows evident seasonal variability. The westward-propagating constituents are branched into multiple beams near 21°N, 121°E, where an anticyclonic eddy exits due to the looping Kuroshio intrusion. In addition, the magnitude of these westward-propagating energy reduces drastically due to the decreasing downstream flux, as previously noted and explained by Lamb and Dunphy (2018). However, relatively small difference occurs east of the LS, due to the slight seasonal variation of the background currents.

The comparison of energy budgets between the summer and winter in the SCS and LS reveals intriguing patterns. Fig. 13 presents a quantitative analysis focusing on key terms such as the regional integrated energy conversion from the barotropic to baroclinic tides (Conv), the divergence of baroclinic tidal energy flux ($DivF_{bc}$) and the energy dissipation of the baroclinic tides ($Diss_{bc}$), along with the baroclinic energy flux at the eastern and western boundaries (Fbc_e and Fbc_w) of the LS. These comparisons provide valuable insights into seasonal variations of tidal energetics. In general, the analysis indicates that the terms of energy budget tend to be higher in summer than in winter. Despite this overall trend, the energy conversion from the barotropic to baroclinic tides in the LS shows a minor difference of around 3% between the two seasons. This suggests that both winter and summer exhibit similar levels of baroclinic tidal energy in the LS. Furthermore, the dissipation is much higher during winter than in summer, which indicates that we cannot assume the energy dissipation will follow the same trend as the energy conversion. This variation in dissipation also highlights the significant role of the seasonally varying background fields. Further analysis reveals that although the energy conversion from barotropic to baroclinic tides in the SCS is only one-third of that in the LS, the regional integrated energy dissipation is twice of that in the LS, and this ratio increases to three times in summer. Overall, the quantitative analysis in Fig. 13 illustrates the seasonal variability of tidal energetics in the SCS and LS, emphasizing the importance of considering the background currents and stratification in tidal energy budget analyses.

4. Discussions

4.1. Evaluation of the LLC4320 simulation

It should be pointed out that the quantitative results presented in this study are unavoidably dependent on model specifics. In the study of Savage et al. (2017), the spectra in tidal and supertidal bands of the 1/48° MITgcm output have been compared to dynamic height variance spectra from McLane profilers in seven regions, including the LS. The results indicate that the model result is well-matched to available data at diurnal and semidiurnal frequencies. Especially, the MITgcm lies closer to the observations in the supertidal band. However, the overestimations of kinetic energy in the diurnal and semidiurnal bands relative to drifter observations exist (Arbic et al., 2018; Yu et al., 2019; Arbic et al., 2022). The overestimations may be due to several significant factors, such as the absence of topographic internal wave drag that accounts for the damping of tidal motions due to breaking small-scale internal tides, which are unresolved in global models. To conduct the quantitative evaluations of the LLC4320 simulation, the results are compared with observations. Firstly, for the barotropic tide, the westward energy fluxes of K_1 and M_2 tides through the LS in summer (August) are compared with the observation results (in April–May) revealed by Beardsley et al. (2004). They reported that the westward fluxes of M_2 and K_1 barotropic tides through the LS are roughly 29 and 28 GW, respectively. The values in this study are 31 GW and 35.41 GW, respectively. The results are thus consistent, even though the values of the LLC4320 simulation are slightly larger, especially for K_1. This discrepancy could also be due to the time difference between the two datasets. Secondly, for the baroclinic tide, the energy fluxes of all baroclinic tides in summer (August) are compared with the observation results (225–250 year-days) revealed by Alford et al. (2011). The energy fluxes at station s4 (s5, s6a, s6b and f1) of the LLC4320 simulation and the observation revealed by Alford

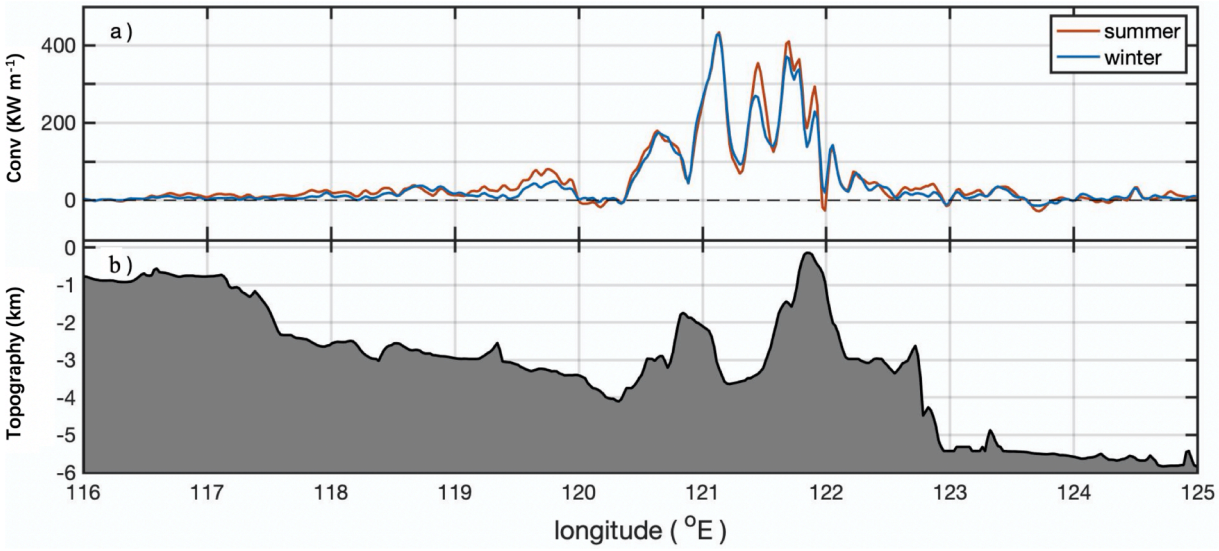

Fig. 11. (a) The meridional integrated (from 17°N to 25°N) energy conversion from the barotropic to baroclinic tides and (b) the topography along 20.25°N.

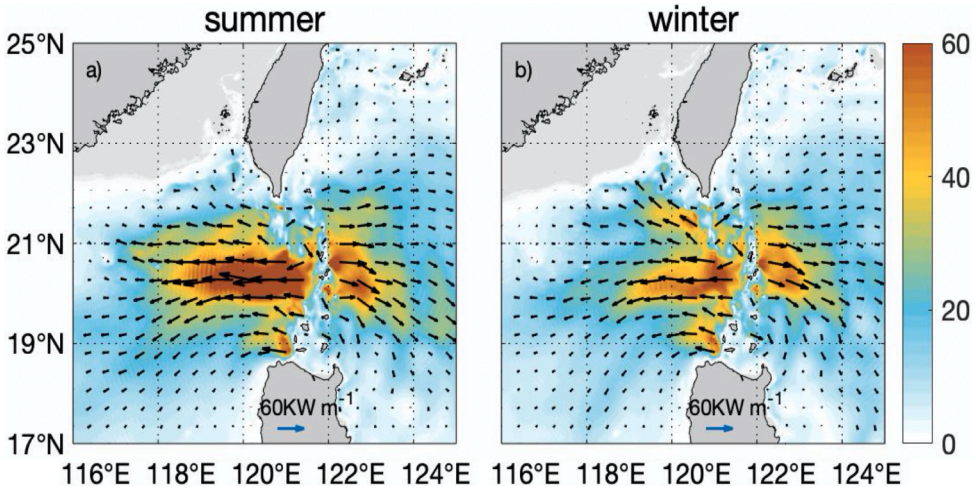

Fig. 12. The monthly-averaged baroclinic tidal energy fluxes in (a) summer and (b) winter (Unit: KW m^{-1}).

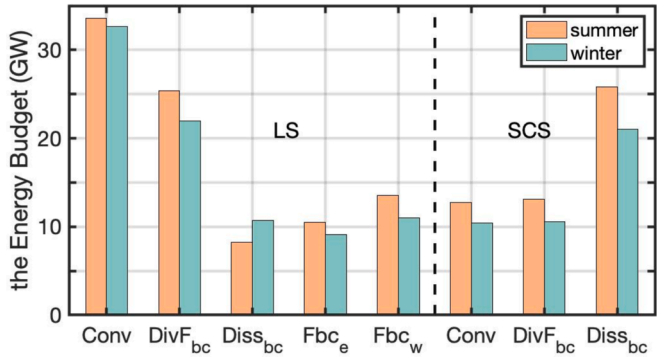

Fig. 13. Comparison of the energy budgets in the SCS and LS, the black dotted box in Fig. 6a and 6b, respectively, for the baroclinic tides between summer and winter, including the regional integrations of energy conversion from barotropic to baroclinic tides (Conv, Unit: GW), the divergence of the energy flux (Div_{bc}, Unit: GW) and the energy dissipation of baroclinic tides ($Diss_{bc}$ Unit: GW), as well as the meridional integrated energy flux on the eastern and western boundaries of dashed box in the LS (i.e., Fbc_e, Fbc_w, Unit: GW).

et al. (2011) are 14.6 (8.0, 36.15, 36.15 and 42.5) and 36.3 (9.2, 36.4, 39 and 41.8) KW m^{-1}, respectively. The values are thus very close. Therefore, the results of the LLC4320 simulation are appropriate for investigating tidal energetics in the SCS.

4.2. Energetics of barotropic tides

Based on the evaluations, it would be informative to examine how tidal energetics calculated from the LLC4320 simulation compare with those from previous mooring observations (Alford et al., 2011), satellite measurements (Zhao, 2014) and idealized model simulations with horizontally homogenous stratifications or without considering the background currents (Jan et al., 2008; Kerry et al., 2013; Niwa and Hibiya, 2004; Wang et al., 2016; Xu et al., 2016).

The barotropic energy budgets calculated from the LLC4320 simulation (Fig. 3) align with previous observations (Beardsley et al., 2004), but show slight differences from the idealized numerical simulations (Wang et al., 2016; Xu et al., 2016; Zu et al., 2008). Based on the Asian Seas International Acoustics Experiment (ASIAEX), Beardsley et al. (2004) report that the westward fluxes of M_2 and K_1 barotropic tides through the Luzon Strait are roughly 29 and 28 GW, respectively. By assimilating Topex/Poseidon altimetry data into a barotropic ocean tide model, Zu et al. (2008) indicated that for M_2 tide, 48.71 GW of energy flows into the LS, and 26.05 GW of energy flows out, with 22.66 GW being dissipated in the LS. For K_1 tide, 44.10 GW of energy flows into the LS, and 19.17 GW of energy flows out, with 23.93 GW being dissipated in the LS. Based on an idealized simulation that uses horizontally homogeneous stratification without considering background currents, Wang et al. (2016) indicate that meridional section-integrated energy fluxes across the LS for M_2 and K_1 barotropic tides reach 35.11 and 24.42 GW, respectively. In this study, we present 31 GW of energy flux for M_2 barotropic tides and 35.41 GW of energy flux for K_1 along the western boundary of the LS, which are more consistent with the observation, although our results (e.g., for the K_1) are slightly larger. In this study, the sum of energy conversion into baroclinic tides and dissipation for M_2 barotropic tides in the LS is 24.85 GW, which is consistent with the results of Zu et al. (2008); however, the sum for K_1 in this study is 15.99 GW, which is modestly smaller than that revealed by Zu et al. (2008). This discrepancy may be due to the different integration areas and the barotropic model they used.

4.3. Energetics of baroclinic tides

An obvious difference in energy conversion between the results revealed in this study (Fig. 5a-d) and those reported in previous studies (e.g., Wang et al., 2016) is the positive energy conversion from the LS to the northeastern shelf-slope (mentioned in Section 3.3) revealed in this study. According to Eq. (10), the energy conversion from the barotropic to baroclinic tides depends not only on the respective magnitude of the pressure perturbation and the vertical barotropic velocity, but also on the phase difference between them. Therefore, there are two main reasons potentially responsible for the differences between the LLC4320 simulation and previous idealized simulations in terms of the conversion rate. Firstly, the seasonal variation of stratification and the stratification modulation due to mesoscale variabilities could affect the magnitude of local pressure perturbation. Secondly, the background currents alter both the arrival time and the propagation paths of the remote baroclinic tides, which could change the phase difference (Kerry et al., 2013).

The present study shows that, ~28% (~19.51 GW) of all barotropic tidal energy input from the NWP is converted to the baroclinic tides for M_2. Comparatively, Niwa and Hibiya (2004) and Jan et al. (2008) gave a slightly smaller estimate, which is ~25% and ~21%, respectively; Kerry et al. (2013) and Xu et al. (2016) reached a larger estimate of ~33%. For K_1, ~12% (~6.52 GW) of barotropic tidal energy input from the NWP is converted to the baroclinic tides in this study, as compared to the ~30% proportion reported by Jan et al. (2008) and Xu et al. (2016). These discrepancies may also be caused by differences in background fields and model resolutions.

Based on idealized simulations, Xu et al. (2016) obtained two regular and concentrated westward beams of M_2 tides. By contrast, our results demonstrate that the energy fluxes are more dispersed and affected by background fields, which is consistent with simulations by Tang et al. (2023) and Xu et al. (2021), who incorporated spatial-temporally varying stratification and the Kuroshio intrusion. Besides, the magnitudes and distributions of the baroclinic tidal energy fluxes revealed in our analysis (Fig. 5e-g and 6a) align with the observational results reported by Alford et al. (2011), who observed tidal energy fluxes of 7.89 GW and 6.05 GW radiating out from the western and eastern sides, respectively. These comparisons all indicate that realistic background fields could alter tidal propagation paths in areas with strong background currents.

Wang et al. (2021) and Niwa and Hibiya (2004) reported that ~35% of the M_2 baroclinic energy generated in the LS is dissipated locally, probably due to the absence of the background circulation and coarse model resolution in the simulations (Kerry et al., 2013; Zilberman et al., 2009). With the background circulation properly considered and the model resolution increased, our estimate (~62%) is closer to the estimate (~66.5%) given by Song and Chen (2020).

Overall, our quantitative analysis reveals that the realistic background fields do affect certain local tidal energetics as well as their associated energy budgets, especially the dissipation of baroclinic tides, particularly in areas with active mesoscale processes.

5. Summary

In this study, we have investigated tidal energetics in the SCS based on a high-resolution numerical simulation with realistic settings. Our main findings can be summarized as follows.

For the barotropic tides, ~61.20% of the energy input into the LS from the NWP is transported into the deep basin of the SCS, with ~19.72% energy converted to baroclinic tides and the other 19.07% dissipated locally. In the SCS, ~59.35% of the barotropic energy input from the LS traverses the deep basin and flows out through the SWS and the SES, with only ~12.20% converted to baroclinic tides and the other ~28.19% dissipated locally. Significantly different behaviors are observed between the K_1 and M_2 barotropic tides. For instance, ~34.92% of the M_2 barotropic energy input from the NWP is lost in the LS, while less than 30% of the K_1 barotropic energy input remains in the LS. It is worth noting that the work rate of K_1 (M_2) tide-generating force is positive (negative) in both the LS and the SCS, indicating that K_1 (M_2) is energized (damped) by the tide-generating force. Besides, the K_1 work rate constitutes ~20% of the divergence of the energy flux in the SCS, and is much larger than the conversion from the barotropic to the baroclinic tides, indicating the significant contribution of local barotropic tidal generation to the overall budget of tidal energy, and highlighting the need to directly consider the tide-generating force in numerical simulations for accurate simulations.

For the baroclinic tides, ~32.75% of the energy conversion from the barotropic to baroclinic tides in the LS is transmitted back to the NWP, while almost all baroclinic tidal energy in the SCS is dissipated, with very little transported away from the southern shelf areas. The main difference between the K_1 and M_2 baroclinic tides is that most (~62.12%) of the M_2 baroclinic energy generated in the LS is dissipated locally, while the majority of the converted baroclinic energy from the K_1 tide (~91.26%) is transported to the SCS and the NWP.

The comparisons among our results of the barotropic and baroclinic tidal energy budgets, those of the previous idealized studies, and the observation-based results suggest that the realistic background fields significantly influence the tidal energetics, as well as the associated energy budgets, especially the energy conversion from the barotropic to baroclinic tides, the propagation paths, and the dissipation of baroclinic tides. This contrast may also be associated with various model configurations, such as parameterizations of unresolved physical processes, bathymetry, and model resolutions. The higher resolution would help resolve finer-scale dynamic processes and the associated wave–mean flow interactions, as well as the topographic scattering. All of these elements contribute to a more accurate estimate of energy transfer and damping. Moreover, higher resolution will play a more important role in shallower regions such as continental shelf. Further research is needed as to how high a resolution is more suitable for studying internal tide dynamics and energetics in the SCS.

The baroclinic tidal energy flux decays away from the source region along the propagation path. The K_1 baroclinic tide has a decay scale of ~404 km. The decay scale of the M_2 baroclinic tide is ~195 km for the northwestward beam and ~127 km for the southwestward beam. The introduction of the decay scale provides a simple metric for measuring the baroclinic tidal energy fluxes in the SCS; this metric has the potential to be incorporated into ocean climate models to characterize tidal mixing.

This study also explores the seasonal variability of tidal energetics in the SCS. The results demonstrate that the terms of energy budget tend to be higher in summer than those in winter. Though the energy conversion from the barotropic to baroclinic tides in the LS shows a minor difference of around 3% between the two seasons, the energy fluxes of baroclinic tides exhibit a huge difference due to the varying background fields caused by the Kuroshio intrusion. Thus, a stronger dissipation exists during winter than summer. All these features highlight the crucial role of background fields in shaping the energetics and dissipation processes of baroclinic tides, emphasizing the importance of incorporating realistic environmental conditions in modeling studies for an accurate representation of tidal dynamics and energetics.

It should be pointed out that the quantitative results presented in this study are unavoidably dependent on model specifics. Therefore, further validations of the results with observations are needed.

CRediT authorship contribution statement

Yonghe Tian: Writing – original draft, Investigation, Formal analysis. **Xiaolin Bai:** Writing – review & editing, Supervision, Project administration, Methodology, Conceptualization. **Chuanyin Wang:** Writing – review & editing. **Zhiyu Liu:** Writing – review & editing, Supervision, Resources, Project administration, Funding acquisition, Data curation, Conceptualization.

Declaration of competing interest

The authors declare that they have no known competing financial interests or personal relationships that could have appeared to influence the work reported in this paper.

Acknowledgments

This work was supported by the National Key R&D Program of China (2023YFE0126700), the National Natural Science Foundation of China (92258301), and the Natural Science Foundation of Fujian Province of China (2021J02005 & 2021J01024). XB's participation in this work was supported by the National Natural Science Foundation of China (42376007). We also sincerely appreciate the detailed comments from four anonymous referees.

Data availability

Data will be made available on request.

References

Alford, M.H., 2003. Redistribution of energy available for ocean mixing by long-range propagation of internal waves. *Nature* 423, 159–162. https://doi.org/10.1038/nature01628.

Alford, M.H., et al., 2011. Energy flux and dissipation in Luzon Strait: Two tales of two ridges. *J. Phys. Oceanogr.* 41, 2211–2222. https://doi.org/10.1175/JPO-D-11-073.1.

Alford, M.H., et al., 2015. The formation and fate of internal waves in the South China Sea. *Nature* 521, 65–69. https://doi.org/10.1038/nature14399.
Ansong, J.K., et al., 2017. Semidiurnal internal tide energy fluxes and their variability in a global ocean model and moored observations. *J. Geophys. Res. Oceans* 122, 1882–1900. https://doi.org/10.1002/2016JC012184.
Arbic, B.K., et al., 2022. Near-surface oceanic kinetic energy distributions from drifter observations and numerical models. J. Geophys. Res. Oceans. https://doi.org/10.1029/2022JC018551.
Arbic, B. K., Coauthors, 2018: A primer on global internal tide and internal gravity wave continuum modeling in HYCOM and MITgcm. *New Frontiers In Operational Oceanography*, E. Chassignet et al., Eds., *GODAE Ocean View*, 307–391, Doi: 10.17125/gov2018.ch13.
Baines, P.G., 1982. On internal tide generation models. *Deep-Sea Res. I* 29, 307–338. https://doi.org/10.1016/0198-0149(82)90098-X.
Beardsley, R.C., et al., 2004. Barotropic tide in the northeast South China Sea. *IEEE J. Oceanic Eng.* 29, 1075–1086. https://doi.org/10.1109/JOE.2004.833226.
Buijsman, M.C., et al., 2014. Three- Dimensional Double- Ridge Internal Tide Resonance in Luzon Strait. *J. Phys. Oceanogr.* 44, 850–869. https://doi.org/10.1175/Jpo-D-13-024.1.
Buijsman, M.C., et al., 2020. On the interplay between horizontal resolution and wave drag and their effect on tidal baroclinic mode waves in realistic global ocean simulations. *Ocean Modell.* 152, 101656. https://doi.org/10.1016/j.ocemod.2020.101656.
Cai, Z., Gan, J., Liu, Z., Hui, C.R., Li, J., 2020. Progress on the formation dynamics of the layered circulation in the South China Sea. *Prog. Oceanogr.* 181, 102246. https://doi.org/10.1016/j.pocean.2019.102246.
Chang, H., et al., 2019. Generation and propagation of M2 internal tides modulated by the Kuroshio northeast of Taiwan. *J. Geophys. Res. Oceans* 124, 2728–2749. https://doi.org/10.1029/2018JC014228.
Chen, G., Hou, Y., Chu, X., 2011. Mesoscale eddies in the South China Sea: Mean properties, spatiotemporal variability, and impact on thermohaline structure. *J. Geophys. Res.* 116, C06018. https://doi.org/10.1029/2010JC006716.
de Lavergne, C., Falahat, S., Madec, G., Roquet, F., Nycander, J., Vic, C., 2019. Toward global maps of internal tide energy sinks. *Ocean Modell.* 137, 52–75. https://doi.org/10.1016/j.ocemod.2019.03.010.
Di Lorenzo, E., Young, W.R., Llewellyn Smith, S.G., 2006. Numerical and analytical estimates of M_2 tidal conversion at steep oceanic ridges. *J. Phys. Oceanogr.* 36, 1072–1084. https://doi.org/10.1175/JPO2880.1.
Egbert, G.D., Ray, R.D., 2000. Significant dissipation of tidal energy in the deep ocean inferred from satellite altimeter data. *Nature* 405, 775–778. https://doi.org/10.1038/35015531.
Farmer, D.M., Alford, M.H., Lien, R.-C., Yang, Y.J., Chang, M.H., Li, Q., 2011. From Luzon Strait to Dongsha Plateau: Stages in the life of an internal wave. *Oceanography* 24 (4), 64–77. https://doi.org/10.5670/oceanog.2011.95.
Farmer, D., Li, Q., Park, J.-H., 2009. Internal wave observations in the South China Sea: The role of rotation and non-linearity. *Atmos.–ocean* 47, 267–280. https://doi.org/10.3137/OC313.2009.
Garrett, C., Kunze, E., 2007. Internal Tide Generation in the Deep Ocean. *Annu. Rev. Fluid Mech.* 39, 57–87. https://doi.org/10.1146/annurev.fluid.39.050905.110227.
Gill, A. E., 1982: *Atmosphere–Ocean Dynamics*. Academic Press, 662 pp.
Guo, Z., Wang, S., Cao, A., Xie, J., Song, J., Guo, X., 2023. Refraction of the M2 internal tides by mesoscale eddies in the South China Sea. *Deep-Sea Res. I* 192 (103), 946. https://doi.org/10.1016/j.dsr.2022.103946.
Huang, X., Wang, Z., Zhang, Z., Yang, Y., Zhou, C., Yang, Q., Zhao, W., Tian, J., 2018. Role of mesoscale eddies in modulating the semidiurnal internal tide: Observation results in the Northern South China Sea. *J. Phys. Oceanogr.* 48, 1749–1770. https://doi.org/10.1175/JPO-D-17-0209.1.
Jan, S., Lien, R.C., Ting, C.H., 2008. Numerical study of baroclinic tides in Luzon Strait. *J. Oceanogr.* 64, 789–802. https://doi.org/10.1007/s10872-008-0066-5.
Kelly, S.M., Lermusiaux, P.F., 2016. Internal-tide interactions with the Gulf Stream and middle Atlantic Bight shelfbreak front. *J. Geophys. Res. Oceans* 121, 6271–6294. https://doi.org/10.1002/2016JC011639.
Kerry, C.G., Powell, B.S., Carter, G.S., 2013. Effects of remote generation sites on model estimates of M2 internal tides in the Philippine Sea. *J. Phys. Oceanogr.* 43, 187–204. https://doi.org/10.1175/JPO-D-12-081.1.
Kerry, C.G., Powell, B.S., Carter, G.S., 2014a. The impact of subtidal circulation on internal tide generation and propagation in the Philippine Sea. *J. Phys. Oceanogr.* 44, 1386–1405. https://doi.org/10.1175/JPO-D-13-0142.1.
Kerry, C.G., Powell, B.S., Carter, G.S., 2014b. The impact of subtidal circulation on internal-tide-induced mixing in the Philippine Sea. *J. Phys. Oceanogr.* 44, 3209–3224. https://doi.org/10.1175/JPO-D-13-0249.1.
Lamb, K.G., 1994. Numerical experiments of internal wave generation by strong tidal flow across a finite amplitude bank edge. *J. Geophys. Res.* 99, 843–864. https://doi.org/10.1029/93JC02514.
Lamb, K.G., Dunphy, M., 2018. Internal wave generation by tidal flow over a two-dimensional ridge: Energy flux asymmetries induced by a steady surface trapped current. *J. Fluid Mech.* 836, 192–221. https://doi.org/10.1017/jfm.2017.800.
Li, Q., Mao, X., Huthnance, J., Cai, S., Kelly, S., 2019. On internal waves propagating across a geostrophic front. *J. Phys. Oceanogr.* 49, 1229–1248. https://doi.org/10.1175/JPO-D-18-0056.1.
Lien, R.-C., Henyey, F., Ma, B., Yang, Y.J., 2014. Large-amplitude internal solitary waves observed in the northern South China Sea: Properties and energetics. *J. Phys. Oceanogr.* 44, 1095–1115. https://doi.org/10.1175/JPO-D-13-088.1.
Lin, H., Liu, Z., Hu, J., Menemenlis, D., Huang, Y., 2020. Characterizing meso-to submesoscale features in the South China Sea. *Prog. Oceanogr.* 188, 102420. https://doi.org/10.1016/j.pocean.2020.102420.
Marshall, J.C., Adcroft, A., Hill, C., Perelman, L., Heisey, C., 1997. A finite-volume, incompressible Navier Stokes model for studies of the ocean on parallel computers. *J. Geophys. Res.* 102, 5753–5766. https://doi.org/10.1029/96JC02775.
Müller, M., 2013. On the space- and time-dependence of barotropic-to-baroclinic tidal energy conversion. *Ocean Modell.* 72, 242–252. https://doi.org/10.1016/j.ocemod.2013.09.007.
Munk, W., Wunsch, C., 1998. Abyssal recipes II: Energetics of tidal and wind mixing. *Deep-Sea Res. I* 45, 1977–2010. https://doi.org/10.1016/S0967-0637(98)00070-3.
Nan, F., Xue, H., Yu, F., 2015. Kuroshio intrusion into the South China Sea: A review. *Prog. Oceanogr.* 137, 314–333. https://doi.org/10.1016/j.pocean.2014.05.012.
Niwa, Y., Hibiya, T., 2004. Three-dimensional numerical simulation of M2 internal tides in the East China Sea. *J. Geophys. Res.* 109, C04027. https://doi.org/10.1029/2003JC001923.
Pickering, A., Alford, M., Nash, J., Rainville, L., Buijsman, M., Ko, D.S., Lim, B., 2015. Structure and variability of internal tides in Luzon Strait. *J. Phys. Oceanogr.* 45, 1574–1594. https://doi.org/10.1175/JPO-D-14-0250.1.
Rainville, L., Lee, C.M., Rudnick, D.L., Yang, K.-C., 2013. Propagation of internal tides generated near Luzon Strait: Observations from autonomous gliders. *J. Geophys. Res. Oceans* 118, 4125–4138. https://doi.org/10.1002/jgrc.20293.
Ray, R.D., Zaron, E.D., 2011. Non-stationary internal tides observed with satellite altimetry. *Geophys. Res. Lett.* 38, L17609. https://doi.org/10.1029/2011GL048617.
Rocha, C.B., Chereskin, T.K., Gille, S.T., Menemenlis, D., 2016. Mesoscale to submesoscale wavenumber spectra in Drake Passage. *J. Phys. Oceanogr.* 46, 601–620. https://doi.org/10.1175/JPO-D-15-0087.1.
Savage, A.C., et al., 2017. Spectral decomposition of internal gravity wave sea surface height in global models. *J. Geophys. Res. Oceans* 122, 7803–7821. https://doi.org/10.1002/2017JC013009.
Simmons, H., Chang, M.H., Chang, Y.T., Chao, S.Y., Fringer, O., Jackson, C.R., Ko, D.S., 2011. Modeling and prediction of internal waves in the South China Sea. *Oceanography* 24, 88–99. https://doi.org/10.5670/oceanog.2011.97.
Simmons, H.L., Jayne, S.R., Laurent, L.C.S., Weaver, A.J., 2004. Tidally driven mixing in a numerical model of the ocean general circulation. *Ocean Modell.* 6, 245–263. https://doi.org/10.1016/S1463-5003(03)00011-8.
Siyanbola, O.Q., Buijsman, M.C., Delpech, A., Renault, L., Barkan, R., Shriver, J.F., Arbic, B.K., McWilliams, J.C., 2023. Remote internal wave forcing of regional ocean simulations near the US West Coast. *Ocean Modell.* 181, 102154. https://doi.org/10.1016/j.ocemod.2022.102154.
Siyanbola, O.Q., Buijsman, M.C., Delpech, A., Barkan, R., Pan, Y., Arbic, B.K., 2024. Interactions of remotely generated internal tides with the U.S. West Coast continental margin. *J. Geophys. Res. Oceans* 129. https://doi.org/10.1029/2023JC020859 e2023JC020859.
Song, P., Chen, X., 2020. Investigation of the internal tides in the Northwest Pacific Ocean considering the background circulation and stratification. *J. Phys. Oceanogr.* 50, 3165–3188. https://doi.org/10.1175/JPO-D-19-0177.1.
Tang, G., Deng, Z., Chen, R., Xiu, F., 2023. Effects of the Kuroshio on internal tides in the Luzon Strait: A model study. *Front. Mar. Sci.* 9, 995601. https://doi.org/10.3389/fmars.2022.995601.
Wang, X., Peng, S., Liu, Z., Huang, R.X., Qian, Y.-K., Li, Y., 2016. Tidal mixing in the South China Sea: An estimate based on the internal tide energetics. *J. Phys. Oceanogr.* 46, 107–124. https://doi.org/10.1175/JPO-D-15-0082.1.
Wang, Y., Xu, Z., Yin, B., Hou, Y., Chang, H., 2018. Long-Range radiation and interference pattern of multisource M2 internal tides in the Philippine Sea. *J. Geophys. Res. Oceans* 123, 5091–5112. https://doi.org/10.1029/2018JC013910.
Wang, Y., Xu, Z., Hibiya, T., Yin, B., Wang, F., 2021. Radiation path of diurnal internal tides in the northwestern Pacific controlled by refraction and interference. *J. Geophys. Res. Oceans* 126. https://doi.org/10.1029/2020JC016972 e2020JC016972.
Wunsch, C., 1975. Internal tides in the ocean. *Rev. Geophys.* 13, 167–182. https://doi.org/10.1029/RG013i001p00167.
Xu, Z., Yin, B., Hou, Y., Xu, Y., 2013. Variability of internal tides and near-inertial waves on the continental slope of the northwestern South China Sea. *J. Geophys. Res. Oceans* 118, 197–211. https://doi.org/10.1029/2012JC008212.
Xu, Z., Liu, K., Yin, B., Zhao, Z., Wang, Y., Li, Q., 2016. Long-range propagation and associated variability of internal tides in the South China Sea. *J. Geophys. Res. Oceans* 121, 8268–8286. https://doi.org/10.1002/2016JC012105.
Xu, Z., Wang, Y., Liu, Z., McWilliams, J.C., Gan, J., 2021. Insight into the dynamics of the radiating internal tide associated with the Kuroshio Current. *J. Geophys. Res. Oceans* 126, e2020JC017018. https://doi.org/10.1029/2020JC017018.
Yu, X., Ponte, A.L., Elipot, S., Menemenlis, D., Zaron, E.D., Abernathey, R., 2019. Surface kinetic energy distributions in the global oceans from a high-resolution numerical model and surface drifter observations. Geophys. Res. Lett. 46 (16), 9757–9766. https://doi.org/10.1029/2019GL083074.
Zaron, E.D., Egbert, G.D., 2014. Time-variable refraction of the internal tide at the Hawaiian Ridge. *J. Phys. Oceanogr.* 44, 538–557. https://doi.org/10.1175/JPO-D-12-0238.1.
Zhang, Z., Zhao, W., Qiu, B., Tian, J., 2017. Anticyclonic eddy sheddings from Kuroshio loop and the accompanying cyclonic eddy in the northeastern South China Sea. *J. Phys. Oceanogr.* 47, 1243–1259. https://doi.org/10.1175/JPO-D-16-0185.1.
Zhao, Z., 2014. Internal tide radiation from the Luzon Strait. *J. Geophys. Res. Oceans* 119, 5434–5448. https://doi.org/10.1002/2014JC010014.
Zhao, Z., Alford, M.H., Girton, J.B., Rainville, L., Simmons, H.L., 2016. Global observations of open-ocean mode-1 M2 internal tides. *J. Phys. Oceanogr.* 46, 1657–1684. https://doi.org/10.1175/JPO-D-15-0105.1.

Zhao, Z., Qiu, B., 2023. Seasonal West-east seesaw of M_2 internal tides from the Luzon Strait. *J. Geophys. Res. Oceans* 128, e2022JC019281. https://doi.org/10.1029/2022JC019281.

Zilberman, N., Becker, J., Merrifield, M., Carter, G., 2009. Model estimates of M2 internal tide generation over Mid-Atlantic Ridge topography. *J. Phys. Oceanogr.* 39, 2635–2651. https://doi.org/10.1175/2008JPO4136.1.

Zu, T., Gan, J., Erofeeva, S.Y., 2008. Numerical study of the tide and tidal dynamics in the South China Sea. *Deep-Sea Res. I* 55, 137–154. https://doi.org/10.1016/j.dsr.2007.10.007.